Journal of Power Sources 280 (2015) 505–515

Contents lists available at ScienceDirect

Journal of Power Sources

journal homepage: www.elsevier.com/locate/jpowsour

# Compatibility between strontium-doped ferrite cathode and metallic interconnects in solid oxide fuel cells

Verónica Miguel-Pérez, Ana Martínez-Amesti*, María Isabel Arriortua*

*Universidad del País Vasco (UPV/EHU), Facultad de Ciencia y Tecnología, Departamento de Mineralogía y Petrología, Sarriena S/N, 48940 Leioa, Vizcaya, Spain*

## HIGHLIGHTS

- Chromium migration from metallic interconnects was studied at 800 and 1000 °C in air.
- Structural changes of $La_{0.6}Sr_{0.4}FeO_3$ cathode are produced by $Cr^{3+}$ substitution.
- ASR of cells in contact with alloys increase after oxidation test.
- The half-cells assembled with Crofer 22 APU and Conicro 4023 W 188 showed the best results.

## ARTICLE INFO

*Article history:*
Received 14 August 2014
Received in revised form
12 January 2015
Accepted 14 January 2015
Available online 15 January 2015

*Keywords:*
Cathode losses
Degradation
High temperature
Bipolar plate
Solid oxide fuel cell

## ABSTRACT

One of the most important issues related to the performance of solid oxide fuel cells (SOFCs) is the chromium poisoning of the perovskite-type materials used as cathodes by the gaseous chromium species from metallic interconnects. In this study, powder mixtures of LSF40-$Cr_2O_3$ were heated at 800 °C and 1000 °C in air and were subsequently analysed by X-ray powder diffraction. For all the mixtures, the crystallisation of $SrCrO_4$ was observed. In addition, the degradation occurring between three alloys with different compositions, Crofer 22 APU, SS430 and Conicro 4023 W 188, as metallic interconnects and $La_{0.6}Sr_{0.4}FeO_3$ (LSF40) ceramic material as a cathode was studied. The results show significant chromium deposition and the formation of $SrCrO_4$, $LaCrO_3$ and $La_2O_3$ that block the active LSF40 electrode surface and degrade the stack (YSZ/SDC/LSF40/Interconnect) performance. LSF40 assembled with SS430 exhibited substantial Cr deposition. The deposition of the Cr species and the reaction with the LSF40 cathode is related to the composition of the oxide scales formed at each metallic interconnect and at the same time is related to the composition of the alloys. The best results obtained were for the half-cell (YSZ/SDC/LSF40) in contact with Conicro 4023 W 188 and Crofer 22 APU after heat treatment in air at 800 °C for 100 h.



## 1. Introduction

The development of new electrolytes, electrodes and interconnect materials for solid-oxide fuel cells (SOFCs) is associated with the reduction of the working temperature (600–800 °C) [1–3]. The doped $ABO_3$ perovskite family of compounds (A = lanthanide group; B = transition metal group) have been extensively used as SOFC cathodes. Pure electronic conducting perovskites such as Sr- and Ca-doped lanthanum manganites have been conventionally used at 800–1000 °C with adequate performance. Currently, mixed ionic–electronic conductors (MIECs), such as $La_{1-x}Sr_xFeO_3$ (LSF), $La_{1-x}Sr_xCoO_3$ (LSC), $Ba_{1-x}Sr_xCo_{0.8}Fe_{0.2}FeO_3$ (BSCF) or $La_{1-x}Sr_xCo_{1-y}Fe_yO_3$ (LSCF), are being investigated because they provide high power densities at lower temperatures [4–6]. However, several studies have shown that iron-based perovskite cathodes react with YSZ electrolyte and form poorly conducting secondary phases which increases the contact resistance of the system. One solution to avoiding the crystallisation of these phases is to include a samaria-doped ceria (SDC) barrier layer between the LSF and YSZ to avoid such reactivity [7,8]. However, several individual cells must be connected in series to form a stack to obtain usable cell voltage and power. Toward this end, interconnects that connect the anode side of a single cell with the cathode side of the adjacent single cell

* Corresponding authors.
*E-mail addresses:* ana.martinez@ehu.es (A. Martínez-Amesti), maribel.arriortua@ehu.es (M.I. Arriortua).

http://dx.doi.org/10.1016/j.jpowsour.2015.01.094
0378-7753/

are used; these interconnects act as a physical barrier to prevent any contact between the reducing and oxidising atmospheres [9,10].

Metallic alloys are currently being investigated as alternatives to ceramic interconnect materials; such alloys would significantly reduce the system cost. The ferritic stainless steels (FSSs) are the most attractive materials for this application because they exhibit high strength and good machinability and are inexpensive to manufacture; they also exhibit high thermal expansion coefficients (TECs) that closely match those of the electrode materials. Moreover, several groups [11–13] have worked with Ni-, Fe- and Co-based superalloys.

In general, superalloys exhibit low high-temperature creep and high fatigue strengths as well as resistance to hot corrosion attack. Cobalt superalloys generally exhibit better weldability, better thermal-fatigue resistance and higher melting points than nickel- and iron-based superalloys [14,15]. However, one problem related to the degradation of SOFC stacks is chromium poisoning of the cathode by the vaporisation of $Cr_2O_3$(s) from the surface of metallic interconnects as $CrO_3$ (gas) or $CrO_2(OH)_2$ (gas) [16–19].

The interaction between metallic interconnects and cathodes such as LSC, LSM and LSCF in SOFCs has been extensively investigated [20,21]. M. Yang et al. [22] investigated the influence of chromium poisoning on the long-term stability of the oxygen exchange kinetics of $La_{0.6}Sr_{0.4}CoO_3$ (LSC40), which exhibits asignificant decrease in its chemical oxygen surface enhancement coefficient. S. P. Jiang et al. [23,24] observed that the gaseous Cr species generated from Fe–Cr alloys can cause rapid performance deterioration of LSM and LSCF cathodes toward the $O_2$ reduction reaction. In addition, they observed significant deposition of Cr species on the cathode, resulting in the formation of strontium chromium oxide columnar structures of $SrCrO_4$ and $Cr_2O_3$. However, $La_{0.6}Sr_{0.4}FeO_3$ (LSF40), which exhibits high electronic and oxide ion conductivities (~200 S $cm^{-1}$) at high temperatures, has been poorly studied as cathode with respect to its contact with metallic materials [25,26].

The aim of this work was to extend previous degradation analysis between LSF40 as cathode and the materials in contact with used in solid oxide fuel cells systems. The improvement of iron-based perovskites in contact with alloys used as interconnect was carried out. The chemical stability and reactivity of $La_{0.6}Sr_{0.4}FeO_3$ (LSF40) perovskite in the presence of $Cr_2O_3$ at different temperatures and in contact with three metallic interconnects with different chemical compositions (Crofer 22 APU, SS430 and Conicro 4023 W 188) at 800 °C in air were conducted. In addition, the electrochemical behaviour of YSZ/SDC/LSF40/interconnect stacks was tested after 100 h at 800 °C in air.

## 2. Experimental

The study was performed using two pre-oxidised Fe–Cr-based alloys, Crofer 22 APU (Thyssenkrupp VDM) and SS430 (Hamilton Precision Metals), and a Co-based superalloy, Conicro 4023 W 188 (Thyssenkrupp VDM GmbH), which were heated at 800 °C for 100 h in air in a Carbolite furnace. The chemical compositions of the starting alloys were analysed by inductively coupled plasma atomic emission spectroscopy (ICP-AES) on a Horiba Yobin Ybon Activa spectrophotometer (Table 1).

**Table 1**
Chemical composition of steel samples (in wt %), as determined by ICP-AES.

| | Cr | Fe | Ni | W | Co | Mn |
|---|---|---|---|---|---|---|
| Crofer 22 APU | 22.19 (2) | 77.29 (1) | – | – | – | 0.52 (1) |
| SS430 | 16.77 (2) | 82.79 (1) | – | – | – | 0.44 (2) |
| Conicro 4023 W 188 | 22.07 (1) | 2.70 (1) | 22.29 (1) | 15.50 (2) | 36.58 (1) | 0.86 (1) |

The samples were oxidized in air at 800 °C for 100 h, as described in Ref. [27].

The materials used in this research were $Cr_2O_3$ powder from Sigma Aldrich; $La_{0.6}Sr_{0.4}FeO_3$ (LSF40) powder as a cathode material and $(ZrO_2)_{0.92}(Y_2O_3)_{0.08}$ (YSZ) disks with a diameter of 25 mm and a thickness of 300 μm from NexTech, Fuel Cell Materials as an electrolyte material; and $Ce_{0.8}Sm_{0.2}O_{1.9}$ powder (SDC) from Praxair Surface Technologies as an interlayer material between the cathode and electrolyte.

For the chromium-poisoning cathode study, two experiments were conducted. In the first experiment, the reactivity between the LSF40 powders and the $Cr_2O_3$ powder was analysed. To this end, LSF40 and $Cr_2O_3$ powders were mixed. The weight ratio between the LSF40 cathode material and $Cr_2O_3$ was 6:1. To assure homogeneity, the powders were mixed with 220 g of 3 mm zirconia ball media and 25 ml of acetone in a 100 cc vessel. The samples were stirred at 125 rpm for 48 h and the solvent was subsequently evaporated. The obtained powders were then used to prepare pellets under a pressure of 6 tons for 1 min using a 13 mm diameter die and 1 g of powder in a Specac uniaxial press. The pellets were sintered in a conventional Carbolite tubular furnace at two different temperatures, 800 and 1000 °C, for 5 h using a heating rate of 3 °C $min^{-1}$.

In the second experiment, the chromium poisoning of symmetrical half-cells (LSF40/SDC/YSZ) by the metallic interconnect was examined in the configuration shown in Fig. 1a. Symmetrical half-cells were prepared following the procedure in Ref. [28].

For degradation studies, the samples were characterised by X-ray diffraction (XRD) at room temperature using a PHILIPS X'PERT PRO automatic diffractometer equipped with Cu $K_\alpha$ radiation source ($\lambda = 1.5418$ Å). The power generator was set to 40 kV and 40 mA. The patterns were recorded in 2θ steps of 0.026° in the range of 20–80°. The preliminary identification of the composition of the oxide surfaces was performed using the X'Pert HighScore Software, version 2003. The diffraction data of the samples were fitted by the Rietveld method using the FULLPROF program [29–31].

The microstructure, compositional analysis and phase distribution of samples were examined by scanning electron microscopy (SEM) on a JEOL JSM-7000F scanning electron microscope equipped with a Schottky field-emission gun (FEG) and an Oxford Inca Pentafet X3 energy-dispersive X-ray analyser. The operating conditions for observing the microstructure using secondary electron signals (SEs) were an accelerating voltage of 5 kV and a current intensity of $1.96 \times 10^{-11}$ A. The compositional energy-dispersive X-ray (EDX) microanalysis was performed using backscattered electron signals (BSEs) at 20 kV and a current intensity of $5.7 \times 10^{-10}$ A with a working distance of 10 mm.

For the cross-section analysis, the samples were embedded in an epoxy resin, polished using standard metallographic techniques and coated with a coal graphite layer (10 nm) deposited with a Quorum Q150 T sputter coater to provide electrical conductivity.

In this study, the Cr content was very difficult to determine using SEM analysis because the principal emission lines of Cr $k_\alpha$ (5.415 keV) overlap with the La $L_\beta$ (5.385 keV) emission lines. To confirm the presence or absence of Cr in cells in contact with pre-oxidised alloys, X-ray photoelectron spectroscopy (XPS) measurements were performed using an XPS spectrometer (SPECS). All XPS spectra were acquired using a monochromatised X-ray source producing Al $K_\alpha$ radiation ($h\nu = 1.486.6$ eV) and were recorded using a SPECS PHOIBOS 150 analyser. The take-off angle of the photoelectrons was 90° with respect to the specimen. The energy resolution was 0.6 eV. Individual high-resolution spectra

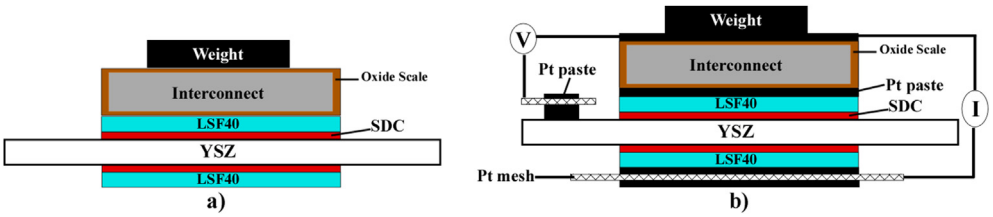


**Fig. 1.** Scheme of the setup for a) the degradation study and b) the ASR measurements.

were taken at 40 eV. Binding energies (BEs) were calibrated against the surface carbon contamination at 284.6 eV.

Finally, for the area-specific resistance (ASR) measurements, symmetrical half-cells (LSF40/SDC/YSZ) with a reference electrode area of 0.25 $cm^2$ and pre-oxidised interconnects (Crofer 22 APU, SS430 and Conicro 4023 W 188) were stacked against each other. A dead weight of 1 kg $cm^2$ was placed on top of this pile to achieve better electrical contact (Fig. 1b).

The electrical conductivity of the symmetrical cells was measured using a current density of 0.3 A $cm^2$ and the 3-point technique in air at 800 °C for 100 h with a Solartron 1260 frequency response analyser.

## 3. Results and discussion

### 3.1. Polycrystalline degradation study

Because the $Cr_2O_3$ is the most abundant oxide in the oxide scale when the metallic interconnects are oxidised at 800 °C in air [27], LSF40-$Cr_2O_3$ mixtures were prepared and sintered at 800 °C and 1000 °C for 5 h in air to determine which phases crystallise and in which proportion at the aforementioned temperatures. This study was performed by XRD. Fig. 2 shows the room-temperature XRD patterns of the mixtures treated in air at three temperatures: 25, 800 and 1000 °C.

After the heat treatment, the LSF40-$Cr_2O_3$ mixtures contained additional phases as $SrCrO_4$, SrO and $SrFe_{12}O_{19}$. The decrease in intensity of the diffraction maxima of the LSF40 cathode material with increasing temperature is due to the partial decomposition of the initial material and the appearance of new phases that resulted from the reactivity with $Cr_2O_3$. To determine the exact proportion of each compound at different processing temperatures, we refined all of the X-ray diffraction patterns using the Rietveld method. The full-profile refinements of the mixtures were performed starting from the atomic coordinates of each phase taken from the Inorganic Crystal Structure Database (ICSD) [32].

Fig. 3 shows the full-profile refinements obtained by Rietveld fittings of the XRD profiles of the mixtures of LSF40 and $Cr_2O_3$ processed at different temperatures. The Rietveld refinements with structural models were approached using the strategy of fixing known values and refining meaningful variables that affect the intensity of the XRD patterns: (1) the scale factor that let us quantify the weight proportion of each phase; (2) the positional parameters (X, Y and Z); (3) the zero point of the detector; (4) the peak shape; (5) the full-width at half-maximum (FWHM) and (6) the asymmetry parameters.

Fig. 3 shows a good agreement between the structural model and the experimental data. The resulting Rietveld analysis (Table 2) demonstrated that, in both heat-treatment cases (800 °C and 1000 °C for 5 h in air), LSF40 reacts with $Cr_2O_3$ to form $SrCrO_4$ as a consequence of the Sr reaction of the LSF40 cathode towards $Cr_2O_3$. In addition, for samples sintered at 1000 °C, new phases were observed, such as SrO and $SrFe_{12}O_{19}$. Striker et al. [33] have confirmed that the strontium hexaferrite phase ($SrFe_{12}O_{19}$) crystallises only at high temperatures.

### 3.2. Cell degradation study

To understand the diffusion processes between LSF40 and metallic interconnects (Crofer 22 APU, SS430 and Conicro 4023 W 188), we assembled symmetrical half-cells (LSF40/SDC/YSZ) with pre-oxidised alloys. The chemical compatibility and contact electrical resistance between the components were investigated at 800 °C for 100 h in air. The room temperature X-ray diffraction patterns of the top of the cells were obtained in air after they were contacted with the alloys (Crofer 22 APU, SS430 and Conicro 4023 W 188) (Fig. 4).

The X-ray diffraction patterns of the cells confirm the interaction between the LSF40 cathode and the metallic interconnects (Crofer 22 APU, SS430 and Conicro 4023 W 188). In addition to the peaks

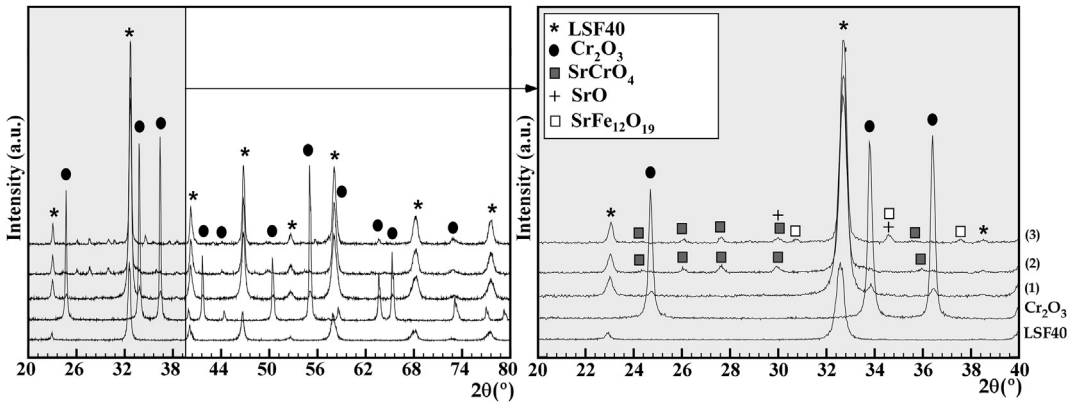


**Fig. 2.** Room-temperature X-ray powder diffraction patterns of LSF40 powder, $Cr_2O_3$ powder and the 6LSF40 + 1$Cr_2O_3$ mixtures treated at different temperatures (1) 25 °C, (2) 800 °C and (3) 1000 °C 0 for 5 h in air.

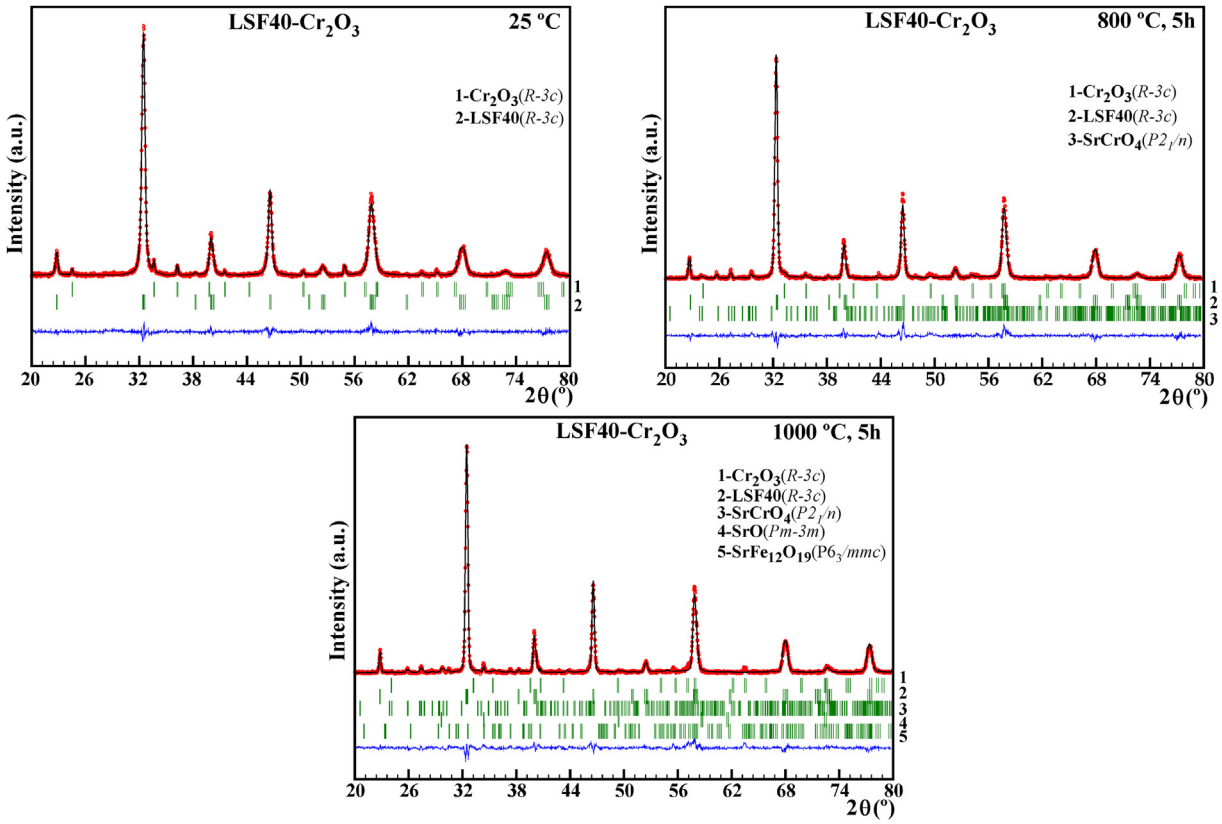


**Fig. 3.** Full-profile refinements for the 6LSF40 + 1$Cr_2O_3$ mixtures at room temperature; the samples were heated at 800 °C or 1000 °C for 5 h in air.

**Table 2**
Proportion of secondary phases calculated by X-ray full profile refinement at different temperatures for (LSF40-$Cr_2O_3$) mixtures.

| Phases (space group) (N°PDF) | 25 °C | 800 °C, 5 h | 1000 °C, 5 h |
|---|---|---|---|
| $La_{0.6}Sr_{0.4}FeO_3$ (R-3c) (83–1961) | 91.29 (4) | 87.59 (6) | 87.03 (1) |
| $Cr_2O_3$ (R-3c) (38–1479) | 8.71 (7) | 6.18 (7) | 0.14 (1) |
| $SrCrO_4$ ($P2_1/n$) (36–0093) | – | 6.23 (4) | 10.36 (6) |
| SrO(Fm-3m) (06–0520) | – | – | 1.12 (5) |
| $SrFe_{12}O_9$ ($P6_3/mmc$) (72–0739) | – | – | 1.35 (4) |

observed in the XRD patterns of the materials that compose the cells (LSF40, SDC and YSZ), additional peaks are also observed in the patterns.

The qualitative analyses revealed the presence of new phases, including $SrCrO_4$, $LaCrO_3$, $La_2O_3$ and the LSF40 cubic phase, in all cases. The intensities of these diffraction maxima are greater in the case of Crofer 22 APU and SS430 than in the case of Conicro 4023 W 188.

In contrast with previous XRD analyses, our XRD analysis of the cells did not indicate the presence of $Cr_2O_3$, SrO or $SrFe_{12}O_{19}$ because these secondary phases crystallise at high temperatures. However, the microstructure and composition of LSF40 surfaces in contact with the three metallic interconnects (Crofer 22 APU, SS430 and Conicro 4023 W 188) was evaluated using SEM. Fig. 5 shows the surface microstructure and the microanalysis at different points of the cells (LSF40/SDC/YSZ) in contact with alloys after oxidation at 800 °C for 100 h in air.

The EDX qualitative analysis (Fig. 5) indicated the existence of

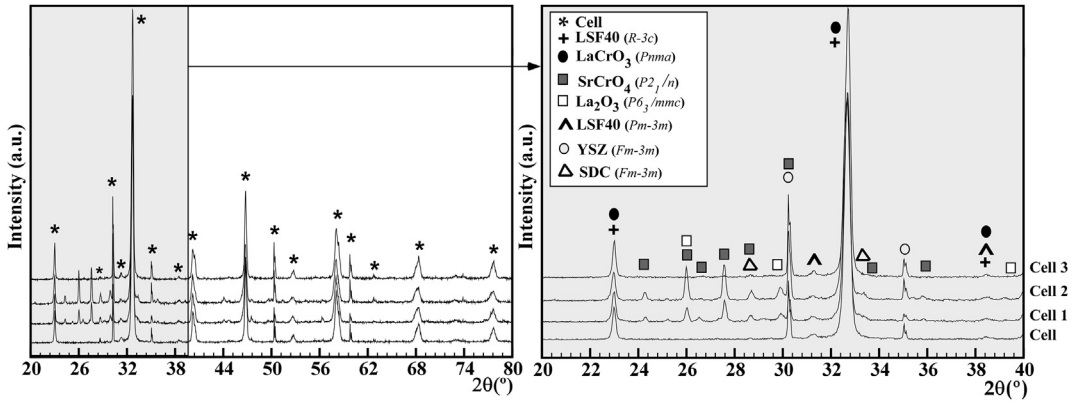


**Fig. 4.** Room-temperature X-ray diffraction patterns of cells (YSZ/SDC/LSF40) in contact with Crofer 22 APU (cell 1), SS430 (cell 2) and Conicro 4023 W 188 (cell 3) after oxidation at 800 °C for 100 h in air. The X-ray diffraction patterns of the cell surfaces after oxidation at 800 °C for 100 h in air are included for reference.

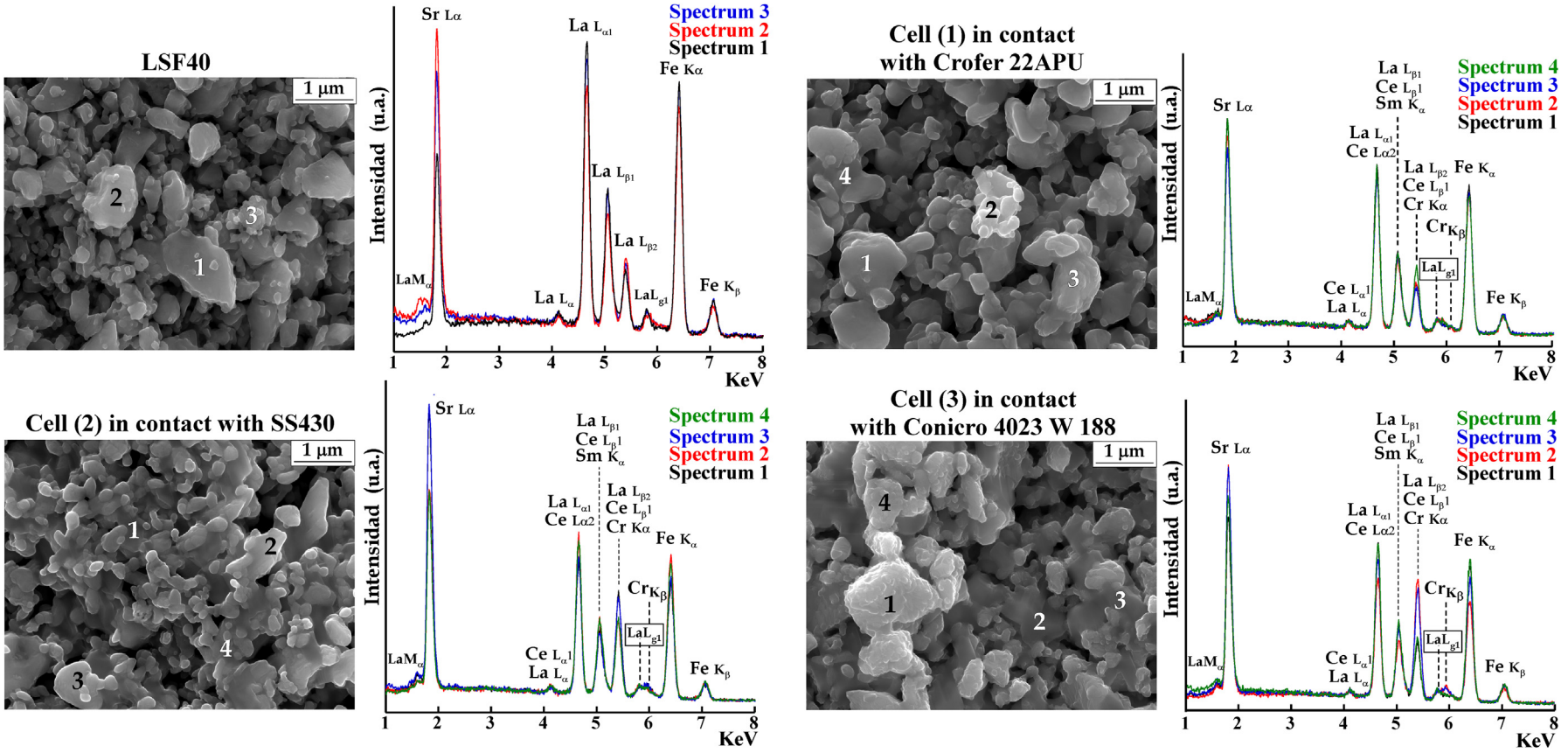


**Fig. 5.** Changes in the surface microstructure, as measured by secondary electrons (SE) signals and EDX analyses at different points of (YSZ/SDC/LSF40) cells in contact with Crofer 22 APU (1), SS430 (2) and Conicro 4023 W 188 (3) after oxidation at 800 °C in air for 100 h. The acquisition parameters for the points were as follows: 20 kV, 25% dead time, and 100 s/point. MEB-FEG micrograph and EDX analysis of the LSF40 surface are included for reference.

the Cr $K_\alpha$ and Cr $K_\beta$ emission peaks in all of the cells in contact with Crofer 22 APU (cell 1), SS430 (cell 2) and Conicro 4023 W 188 (cell 3). Grain 4 for cell 1, grain 3 for cell 2 and grain 2 for cell 3 contain greater amounts of Cr and Sr compared to the other particles, resulting in the formation of the $SrCrO_4$ phase, in good agreement with the XRD analysis results. In addition, these grains exhibit a different morphology. A similar composition was also observed in other particles; however, the intensity of Cr was relatively lower.

To determine the Cr deposition and migration along the LSF40 cathode, an elemental distribution map analysis was performed on the cross-section of the cells in contact with the alloys (Crofer 22 APU, SS430 and Conicro 4023 W 188) after the cells were oxidised in air at 800 °C for 100 h (Fig. 6).

BSE SEM images revealed that the Cr content in LSF40 was greater in cells that were in contact with the ferritic stainless steels (Crofer 22 APU and SS430). The Cr and Sr exhibited very similar distributions along the LSF40 cathode layer, which means that the Sr and Cr were together forming the $SrCrO_4$ oxide observed by XRD. This oxide formed primarily on the LSF40 surface. However, the cell in contact with Conicro 4023 W 188 exhibited less Cr migration along the LSF40 cathode. Moreover, Cr deposits were observed along the SDC interlayer as $Cr_2O_3$ oxide.

To confirm the presence of Cr along the cathode layer, we compared the experimental and reconstructed spectra, taking into account that the principal emission peak of Cr $K_\alpha$ (5.415 keV) overlaps the La $K_\alpha$ (5.385 keV) emission peak. The INCA350 software from Oxford was used to reconstruct the spectra. Fig. 7 shows the experimental spectrum and the reconstructed spectrum for cells (1–3) considering that Cr is not present.

A comparison of the experimental and reconstructed spectra reveals that the Cr $K_\alpha$ (5.415 keV) and Cr $K_\beta$ (5.947 keV) energy peaks in the experimental spectra indicate the presence of Cr in the cells (1–3). However, to verify the Cr poisoning on the LSF40 cathode material with greater precision, the surfaces of the cells in contact with alloys were investigated by XPS. Fig. 8 presents the survey XPS spectra of the LSF40 in cells in contact with the metallic materials.

According to these results, the LSF40 surfaces in contact with the three alloys (Crofer 22 APU, SS430 and Conicro 4023 W 188) contained mainly La, Sr, Fe and O, as well as a small amount of Cr. All of the core-level intensities were corrected for XPS sensitivity factors and were plotted as a function of the binding energy (BE). The resulting plots indicated the presence of Cr in all of the samples.

Fig. 9 presents a comparison of the high-resolution XPS spectra for the La (3d), Cr (2p), Sr (3d) and O (1s) observed in the cells in contact with alloys.

The La-3d XPS spectrum showed two doublets. The La-3d states in the XPS spectra are split not only because of a spin-orbit interaction into two lines $3d_{5/2}$ and $3d_{3/2}$, but each line is additionally split because of a transfer of an electron from oxygen ligands to the La-4f orbital. The observed two doublets can be assigned to two different lanthanum oxides. A doublet near the BEs of 833.7 eV and 850.0 eV, corresponding to $La_2O_3$ and another near of 835.8 eV and 855.0 eV, corresponding to $La_xO_y$, which can be assigned to the LSF40 and $LaCrO_3$ phases [34,35].

The Cr-2p XPS spectra contain a doublet whose binding energies are 579.0 and 589.3 eV, which can be assigned to the $Cr^{6+}$ species. However, the lower-BE positions of 576.5 and 586.6 eV correspond to $Cr^{3+}$. The +6 valence state of the Cr ion indicates the existence of phases such as $CrO_3$ or $SrCrO_4$ [36–38]. The Sr-3d and O-1s XPS spectra each show one main emission line at approximately 135.8 and 529.5 eV, respectively. The Sr-3d XPS spectra indicate similar

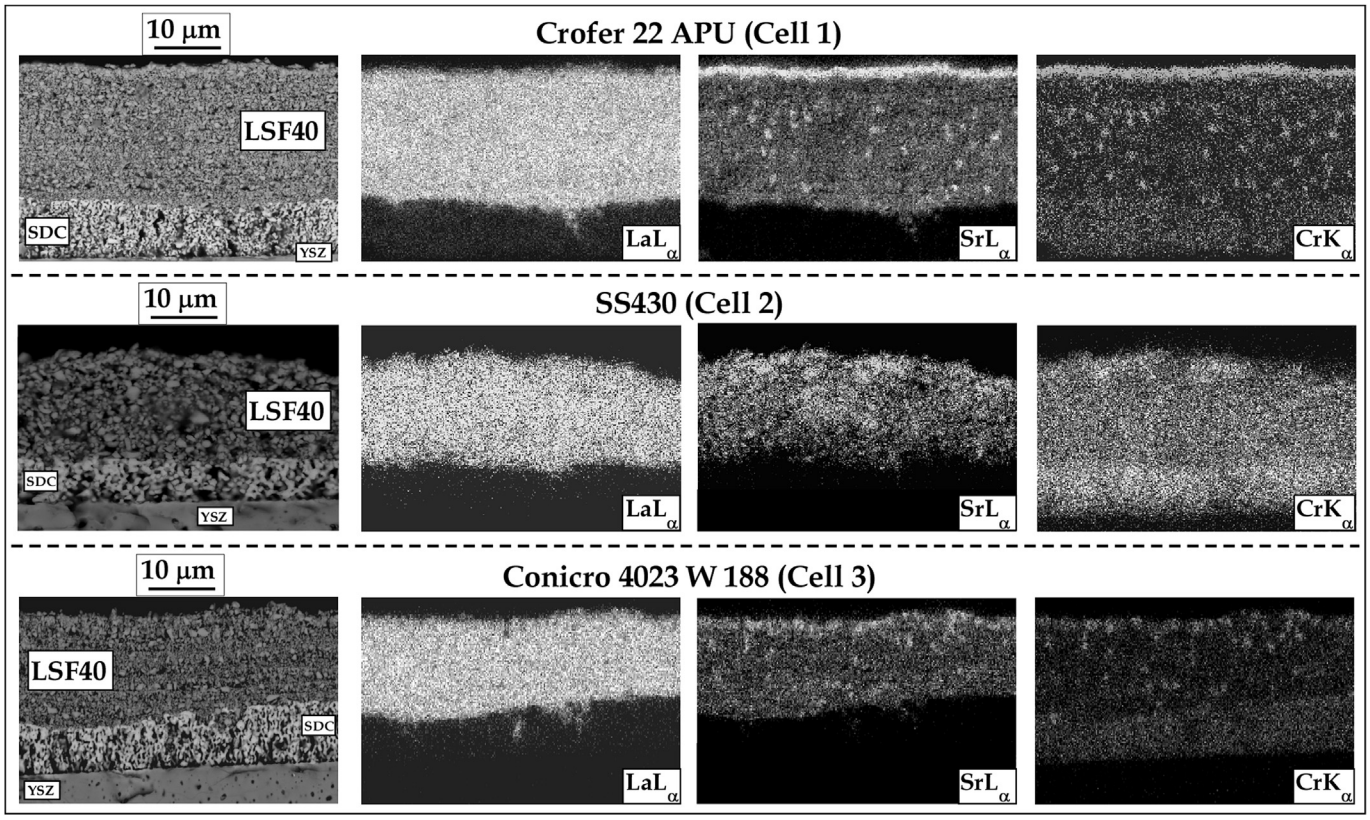


**Fig. 6.** Cross-sectional BSE images and the corresponding EDX elemental distribution map of cells in contact with alloys at 800 °C in air for 100 h.

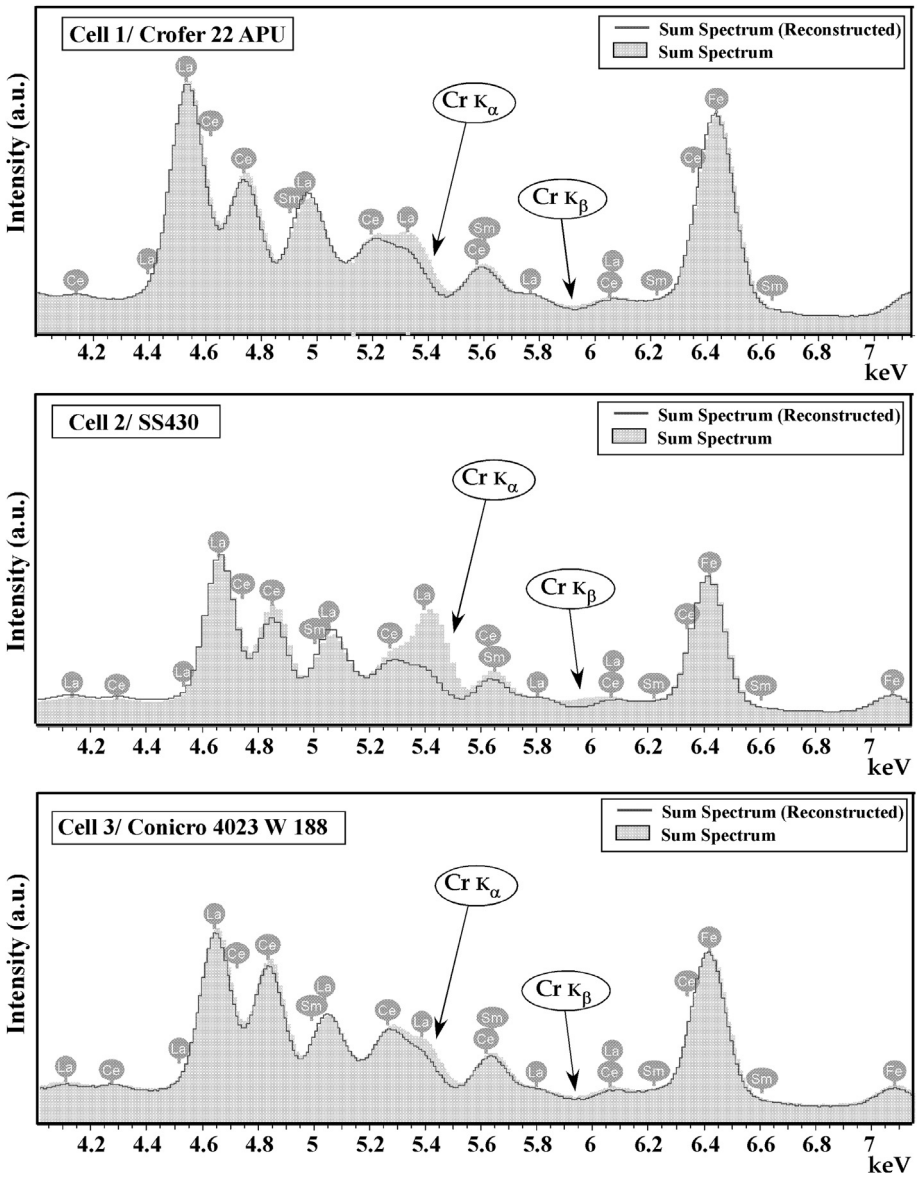


**Fig. 7.** Experimental and reconstructed EDX spectra of cells (1–3) after oxidation at 800 °C for 100 h.

results for cells 1 and 2; these peaks were accompanied by a small shoulder peak due to the presence of a doublet at approximately 133.6 eV. In addition, some differences were noted in the O-1s and Sr-3d spectra of cells in contact with SS430; these differences were due to the greater amount of $SrCrO_4$ [39,40].

Finally, to evaluate the influence of the formed solid solution phases at the cathode material, the electrical performance of the cells was measured after 100 h at 800 °C in air. Fig. 10 shows the ASR as a function of time at 800 °C in air for selected metallic materials used as interconnects and for the resulting cell (LSF40/SDC/YSZ).

The electrochemical results show that cells that were in contact with ferritic stainless steels (Crofer 22 APU and SS430) gave the highest ASR values, whereas the contact constructed of a Co-based superalloy (Conicro 4023 W 188) led to the lowest contact resistance after heat treatment. The values of the electrical resistance for the system with Crofer 22 APU, SS430 and Conicro 4023 W 188 increased to 0.772, 0.354 and 0.098 Ω $cm^2$ after 100 h, respectively. The overall ASR values were determined by the initial ASR (0 h) and the change in ASR over time (100 h), both of which depend primarily on the electronic and ionic conductivity of the oxidation resistance of the substrate metal, the oxide subscale properties and possible interfacial interactions between the cell and the metallic materials.

The increased resistance may be due to the presence of secondary phases, such as $SrCrO_4$, $La_2O_3$ and $LaCrO_3$, which exhibit minor electrical conductivity. However, the ASR value of the cell assembled with the Conicro 4023 W 188 decreased after 20 h because of the formation of $(Co, Cr, Mn)_3O_4$ between the cell and superalloys, which increased the electrical conductivity [27]. $(Co, Cr, Mn)_3O_4$ is more electrically conductive than the $(Fe, Cr, Mn)_3O_4$ spinel phase formed in ferritic stainless steels (Crofer 22 APU and SS430).

The ASR values of cells assembled with Crofer 22 APU, SS430 and Conicro 4023 W 188 are 1.76, 1.85 and 1.63 Ω $cm^2$, respectively, after oxidation for 100 h. The increase in the ASR value of cell 2 (in contact with SS430) is attributed to increased chromium poisoning of the LSF40.

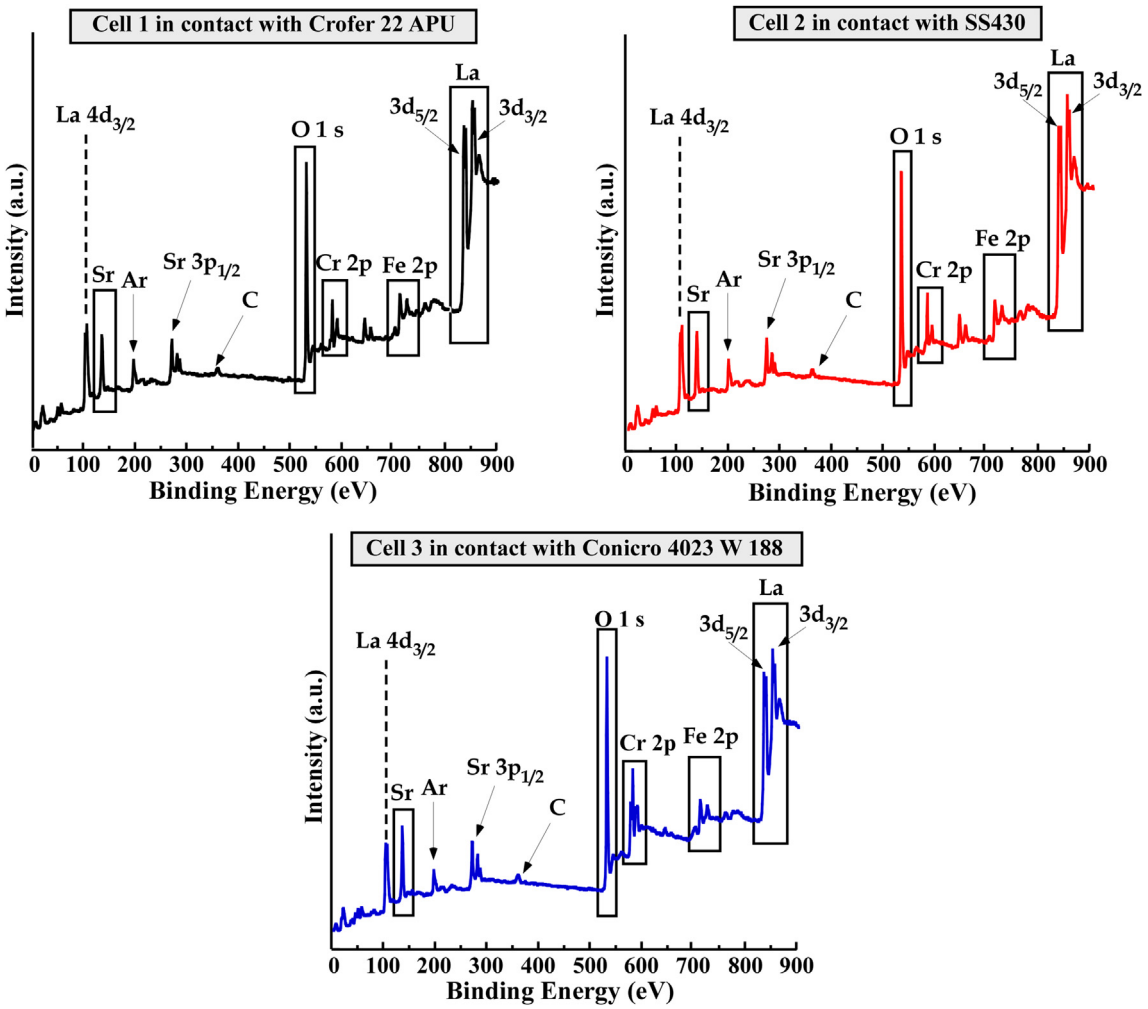


**Fig. 8.** XPS spectra of cell (YSZ/SDC/LSF40) surfaces in contact with interconnects (Crofer 22 APU, SS430 and Conicro 4023 W 188) after oxidation at 800 °C for 100 h in air.

Taking into account the obtained results and the results of several previously published reports [41], we concluded that the deposition of Cr species in the system (LSF40/SDC/YSZ/Interconnect) is significant under SOFC operating conditions, as shown in Fig. 11.

The $SrCrO_4$ phase can be produced by two mechanisms: solid-phase diffusion and vapour deposition of volatile Cr species from metallic interconnects. In both mechanisms, the nucleation agent is identified to be SrO that exists and/or has been segregated at the surface of the LSF40 cathode. The $SrCrO_4$ solid-state diffusion deposition mechanism can be expressed to according to Eq. (1):

$$3SrO(s) + \left(M, Cr^{6+}\right)_3 O_4(s) + 19/2\ O_2(g) \rightarrow 3SrCrO_4(s) + 3/2\ M_2O_3(s) \quad (1)$$

The oxide scale formed in the studied alloys (Crofer 22 APU, SS430 and Conicro 4023 W 188) consisted mainly of chromia ($Cr_2O_3$) and a spinel phase with an $(M, Cr)_3O_4$ composition, where M represents Fe, Mn and/or Co [27]. The interaction between SrO and the $(M, Cr^{6+})_3O_4$ spinel phase would lead to the formation of $SrCrO_4$ and a $M_2O_3$ oxide, where M is Fe, Mn and/or Co. However, in the case of $SrCrO_4$ formation by vapour deposition of Cr species, the mechanism can be represented according to Eqs. (2) and (3):

$$Cr_2O_3\,(s) + 3/2\ O_2\,(g) \rightarrow 2CrO_3\,(g) \quad (2)$$

$$CrO_3\,(g) + SrO\,(s) \rightarrow SrCrO_4\,(s) \quad (3)$$

Volatile Cr gaseous species, such as $CrO_3$, are produced by vaporisation of $Cr_2O_3$ oxide from the interconnects (Eq. (2)). The $SrCrO_4$ phase is identified by the reaction between $CrO_3$ (g) and SrO (Eq. (3)).

$SrCrO_4$ is non-conductive and its formation leads to decreases in both the cathode conductivity and the cathode porosity. In addition, the $LaCrO_3$ substitution reaction always competes with the $SrCrO_4$ precipitation reaction. $LaCrO_3$ can be formed by solid-phase reaction between $Cr_2O_3$ from the oxide scale of alloys and $La_2O_3$ (Eq. (4)) and/or by the reaction between the LSF40 cathode and $CrO_3$ (g) (Eq. (5)):

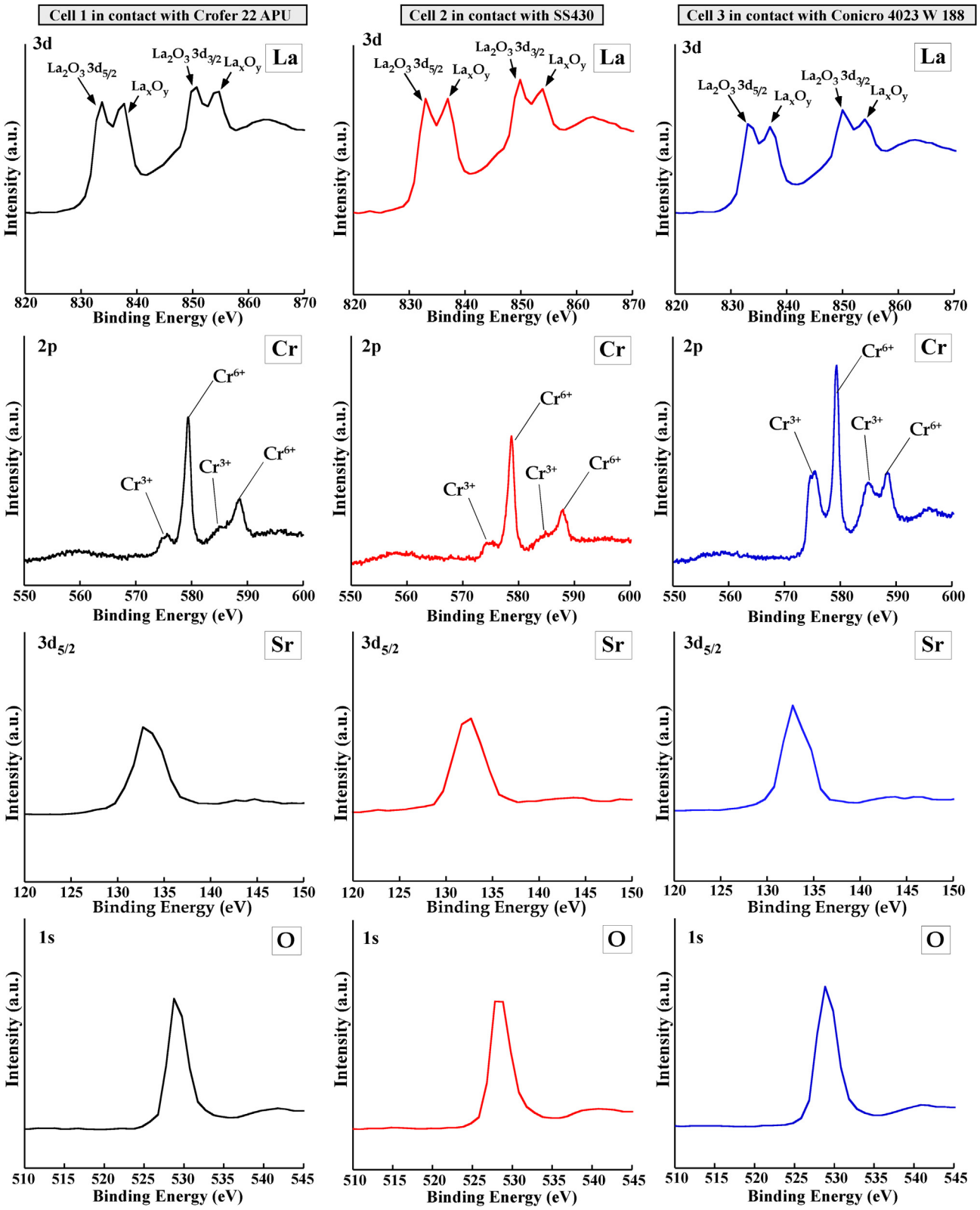


**Fig. 9.** High-resolution XPS spectra of (a) La 3d, Cr 2p, Sr $3d_{5/2}$ and O 1s in cell (YSZ/SDC/LSF40) surfaces in contact with interconnects (Crofer 22 APU, SS430 and Conicro 4023 W 188) after oxidation at 800 °C for 100 h in air.

$$La_2O_3\,(s) + Cr_2O_3\,(s) \rightarrow LaCrO_3\,(s) \quad (4)$$

$$(La, Sr)FeO_3 + CrO_3\,(g) \rightarrow LaCrO_3\,(s) + y\,(La, Sr)FeO_3 \quad (5)$$

The formation of $LaCrO_3$ is difficult to verify because its lattice parameters are similar to those of the LSF40 cathode. This degradation of cells can be induced by a partial symmetry change of the trigonal form of the $(La, Sr)FeO_3$ cathode material to orthorhombic

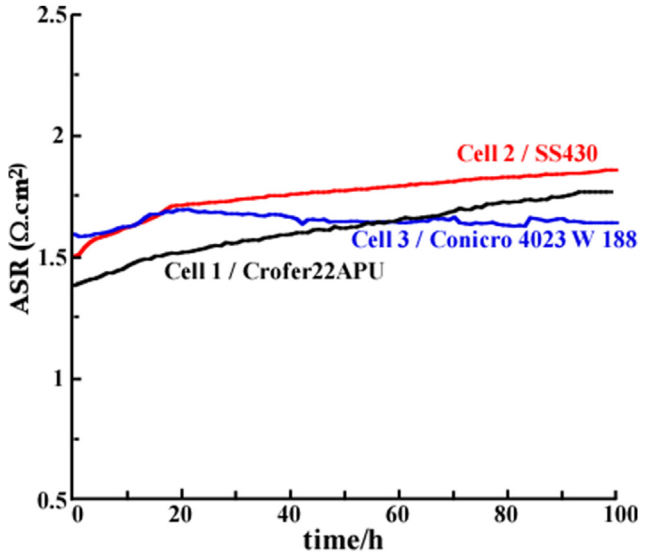


**Fig. 10.** ASR measurements of cells (YSZ/SDC/LSF40) with Crofer 22 APU (1), SS430 (2) and Conicro 4023 W 188 (3) at 800 °C for 100 h in air.

$LaCrO_3$. In addition, $LaCrO_3$ substitution reaction always competes with the $SrCrO_4$ precipitation process. The formation of $SrCrO_4$ is thermodynamically favoured in cathodes that contain less-stable tetravalent ions ($Fe^{4+}$ or $Co^{4+}$) [42].

In contrast, substitution in the SDC interlayer is not possible because of the different atomic radii of $Cr^{3+}$ (0.62 Å), $Ce^{4+}$ (1.14 Å) and $Sm^{3+}$ (1.24 Å). Therefore, $Cr_2O_3$ is deposited at the TPB (Fig. 11). Chemical deposition of $Cr_2O_3$ can occur and is affected by the substrate material, which may be due to the thermodynamic and/or catalytic properties of the cathode material [43,44].

Taking into account the results and the proposed mechanisms of chromium diffusion, we conclude that the deposition of the Cr species and the reaction with the LSF40 cathode is related to the composition of the oxide scale at each interconnect. The oxide scales in Crofer 22 APU, SS430 and Conicro 4023 W 188 consist of two oxide layers: a $(Fe,Cr,Mn)_3O_4$ spinel top layer and an inner ($Cr_2O_3$) chromia layer. Moreover, a $(Co,Cr,Mn)_3O_4$ spinel layer appears on top in the case of Conicro 4023 W 188. LSF40 reacts more with SS430 than with Crofer 22 APU and Conicro 4023 W 188 because its oxide scale consists primarily of $Cr_2O_3$, which is less electrically conducting; furthermore, SS430 has a lower oxidation resistance, which results in the formation of greater amounts of Cr species at the LSF40 surface.

## 4. Conclusions

In this study, we demonstrated the deposition of different compositions of Cr species in $La_{0.6}Sr_{0.4}FeO_3$ (LSF40) when it is in contact with chromia ($Cr_2O_3$) and three metallic materials (Crofer 22 APU, SS430 and Conicro 4023 W 188).

The reactivity of LSF40-$Cr_2O_3$ depends on the sintering temperature and the formation of the $SrCrO_4$ phase is observed after oxidation at 800 °C or 1000 °C in air. At 1000 °C, the additional formation of SrO and $SrFe_{12}O_{19}$ phases was observed because of the partial decomposition of the initial LSF40 cathode. The amount of $SrCrO_4$ phase formed is greater in the case of the LSF40 cathode deposited on ferritic stainless steels, SS430, which exhibits greater Cr vaporisation.

XRD and XPS analysis confirmed the interaction between the cell (YSZ/SDC/LSF40) and the metallic interconnects and allowed the crystallised secondary phases to be identified as a consequence of the Cr vaporisation or migration. The Cr deposition and the formation of $SrCrO_4$, $LaCrO_3$ and $La_2O_3$ can block the active LSF40 electrode surface and degrade the stack (YSZ/SDC/LSF40/Interconnect) performance. Small amounts of Cr phases appeared on the LSF40 cathode assembled with Conicro 4023 W 188. Moreover, the stack formed for YSZ/SDC/LSF40/Conicro 4023 W 188 exhibited the best results during the ASR tests because of the greater oxidation resistance of the Co-based superalloy and the greater electrical conductivity of its oxide scale formed between the cell and alloy.

The deposition of the Cr species and the reaction with the LSF40 cathode is related to the composition of the oxide scales formed at each metallic interconnect and at the same time is related to the composition of the alloys. Iron-based perovskites have a better behaviour when they are in contact with low iron content alloys and with content on other elements as cobalt.

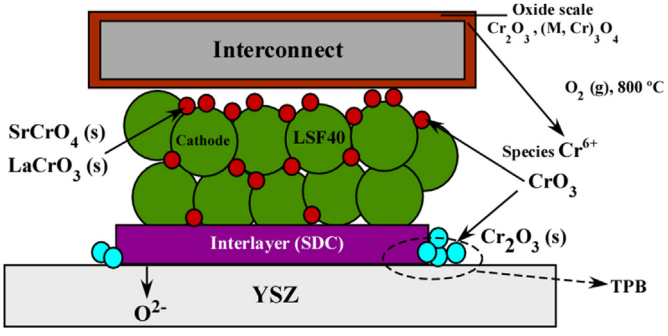


**Fig. 11.** Schematic diagram of Cr poisoning in the system (LSF40/SDC/YSZ/Interconnect).

## Acknowledgements

This work has been financially supported by the Ministerio de Ciencia e Innovación (MAT2010-15375 and Consolider-Ingenio 2010 CSD2009-00013), by Dpto. Industria, Innovación, Comercio y Turismo (SAIOTEK 2013 programme) and by Dpto. Educación, Política Lingüística y Cultura (IT-630-13) of the Basque Government. The authors wish to thank Ikerlan's Fuel Cell group (Miñano, Álava) and the technician of SGIker, Dra. M. B. Sánchez-Ilárduya for the XPS measurements. V. Miguel-Pérez wishes to thank UPV/EHU for funding.

## References

[1] J. Molenda, K. Swierczek, W. Zajac, J. Power Sources 173 (2007) 657–670.
[2] D.J.L. Brett, A. Atkinson, N.P. Brandon, S.J. Skinner, Chem. Soc. Rev. 37 (2008) 1568.
[3] A.J. Jacobson, Chem. Mater. 22 (2010) 660–674.
[4] A. Écija, Óxidos Mixtos Tipo Perovskita $Ln_{0.5}M_{0.5}FeO_{3-\delta}$ (Ln=La, Sm, Nd, Gd; M= Ba, Sr) para su Aplicación como Cátodos en Pilas SOFC, PhD thesis, UPV/EHU, Leioa,, Spain, 2012.
[5] C. Sun, R. Hui, J. Roller, J. Solid State Electrochem 14 (2010) 1125–2114.
[6] J. Richter, P. Holtappels, T. Graule, T. Nakamura, L.J. Gauckler, Monatsh. Chem. 140 (2009) 985–999.
[7] S. Simmer, M. Anderson, J. Bonnett, J. Stevenson, Solid State Ionics 175 (2004) 79–81.
[8] A. Martínez-Amesti, A. Larrañaga, L.M. Rodríguez-Martínez, A.T. Aguayo, J.L. Pizarro, M.L. Nó, A. Laresgoiti, M.I. Arriortua, J. Electrochem. Soc. 156 (2009) B856–B861.
[9] K. Hilpert, W.J. Quaddakers, L. Singheiser, in: W. Vielstich, H.A. Gasteiger, A. Lamm (Eds.), Handbook of Fuel Cells Fundamentals, Technology and Applications, vol. 4, John Wiley & Sons, New Jersey, USA, 2003, pp. 1037–1051.
[10] W.Z. Zhu, S.C. Deevi, Mater. Sci. Eng. A 348 (2003) 227–243.
[11] T. Henhoeffer, X. Huang, S. Yandt, d. Seo, P. Au, J. Mater. Sci. Technol. 25 (7) (2009) 840–850.
[12] Y.C. Ma, X.J. Zhao, M. Gao, K. Liu, J. Mater. Sci. Technol. 27 (2011) 841–845.
[13] H. Lefaix-Jeuland, L. Marchetti, S. Perrin, M. Pijolat, M. Sennour, R. Molins, Corros. Sci. 53 (2011) 3914–3922.
[14] J. Wu, X. Liu, J. Mater. Sci. Technol. 26 (4) (2010) 293–305.
[15] J.W. Fergus, Mater. Sci. Eng. A 397 (2005) 271–283.
[16] G. Kaur, K. Singh, O.P. Pandey, D. Homa, B. Scott, G. Pickrell, J. Power Sources

240 (2013) 458–470.
[17] Z. Yang, K.D. Meinhardt, J.W. Stevenson, J. Electrochem. Soc. 150 (8) (2003) A1095–A1101.
[18] G. Kaur, V. Kumar, O.P. Pandey, K. Singh, J. Electrochem. Soc. 159 (3) (2012) B277–B284.
[19] S.-B. Sohn, S.-Y. Choi, J. Am. Ceram. Soc. 87 (2) (2004) 254–260.
[20] E. Konysheva, J. Mertens, H. Penkalla, L. Singheiser, K. Hilpert, J. Electrochem. Soc. 154 (2007) 1252–1264.
[21] J. Malzbender, P. Batfalsky, R. Vaβen, V. Shemet, F. Tietz, J. Power Sources 201 (2012) 196–203.
[22] M. Yang, E. Bucher, W. Sitte, J. Power Sources 196 (2011) 7313–7317.
[23] X. Montero, W. Fischer, F. Tietz, D. Stöver, M. Cassir, I. Villarreal, Solid State Ionics 180 (2009) 731–737.
[24] S.P. Jiang, S. Zhang, Y.D. Zhen, J. Electrochem. Soc. 153 (2006) 127–132.
[25] A. Morán-Ruíz, K. Vidal, A. Larrañaga, M.I. Arriortua, Fuel Cells 13 (2013) 398–403.
[26] T. Horita, Y. Xiong, H. Kishimoto, K. Yamaji, M.E. Brito, H. Yokokawa, J. Electrochem. Soc. 157 (2010) B614–B620.
[27] V. Miguel-Pérez, A. Martínez-Amesti, M.L. Nó, A. Larrañaga, M.I. Arriortua, Corros. Sci. 60 (2012) 38–49.
[28] V. Miguel-Pérez, A. Martínez-Amesti, M.L. Nó, A. Larrañaga, M.I. Arriortua, J. Power Sources 243 (2013) 419–430.
[29] H.M. Rietveld, Acta Crystallogr. 22 (1967) 151–152.
[30] H.M. Rietveld, J. Appl. Crystallogr. 2 (1969) 65–71.
[31] J. Rodríguez-Carvajal, Fullprof, "Rietveld Pattern Matching Analysis of Powder Patterns", 2009. Grenoble.
[32] Inorganic Crystal Structure Database, ICSD for WWW, Fachin Formations Zentrum, Karlsruhe, Alemania, 2004.
[33] T. Striker, J.A. Ruud, Y. Gao, W.J. Heward, C. Steinbruchel, Solid State Ionics 178 (2007) 1326–1336.
[34] Q.-H. Wu, M. Liu, W. Jaegerman, Mater. Lett. 59 (2005) 1480–1483.
[35] C.-L. Chu, J.-Y. Wang, S. Lee, Int. J. Hydrog. Energy 33 (2008) 2536–2546.
[36] A. Vesel, M. Mozetic, A. Drenik, N. Hauptman, M. Balat-Pichelin, Appl. Surf. Sci. 255 (2008) 1759–1765.
[37] R.-H. Jung, H. Tsuchiya, S. Fujimoto, Corros. Sci. 58 (2012) 62–68.
[38] B. Hua, Y. Kong, W. Zhang, J. Pu, B. Chi, L. Jian, J. Power Sources 196 (2011) 7627–7638.
[39] G. Majkic, M. Mironova, L.T. Wheeler, K. Salama, Solid State Ionics 167 (2004) 243–254.
[40] Y.-M. Kim, X. Chen, S.P. Jiang, J. Bae, J. Electrochem. Soc. 159 (2012) B185–B194.
[41] S.P. Jiang, Y. Zhen, Solid State Ionics 179 (2008) 1459–1464.
[42] H. Yokokawa, T. Horita, N. Sakai, K. Yamaji, M.E. Brito, Y.-P. Xiong, H. Kishimoto, Solid State Ionics 177 (2006) 3193–3198.
[43] J.J. Bentzen, J.V.T. Høgh, R. Barfod, A. Hagen, Fuel Cells 9 (2009) 823–832.
[44] H. Gu, H. Chen, Y. Zheng, L. Guo, Int. J. Hydrog. Energy 35 (2010) 2457–2462.